ATLAS CONF Note

ATLAS-CONF-2023-059

5th September 2023

Charged-hadron yield measurements in photo-nuclear collisions using 5.02 TeV Pb+Pb data with ATLAS

The ATLAS Collaboration

This note presents the analysis of charged-hadron measurements in photo-nuclear collisions using 1.73 nb^{-1} of 5.02 TeV Pb+Pb data collected in 2018 by ATLAS. Candidate photo-nuclear events are selected and background events rejected using a combination of zero degree calorimeter measurement, pseudorapidity gap, and tracking information. The yield of charged hadrons as a function of transverse momentum (p_{T}) and pseudorapidity (η) is measured in these photo-nuclear collisions as a function of charged-particle multiplicity. The results are compared with 0.10 nb^{-1} of 5.02 TeV p+Pb data collected in 2016 by ATLAS using similar charged-particle multiplicity selections. These photo-nuclear measurements are important for constraining the photon energy distribution and particle production in Monte Carlo models such as DPMJET-III. Additionally, the results are important to test whether such photo-nuclear collisions may produce small droplets of quark-gluon plasma that flow hydrodynamically.

ATLAS-CONF-2023-059
19 September 2023

Contents

1 Introduction

When ultra-relativistic beams of lead nuclei are brought into collision, the typical processes studied are those for which the nuclei have an impact parameter (b) smaller than twice the nuclear radius ($b < 2R$). These so-called hadronic collisions are understood to create a large region of quark-gluon plasma and produce a large number of particles in the final state. However, the strong electromagnetic (EM) fields of the fully ionized nuclei can also induce interactions when the nuclei have significantly larger impact parameters [1, 2]. In the equivalent photon approximation, these strong EM fields correspond to a flux of quasi-real, high-energy photons. Importantly, the nuclei can produce high-energy photons coherently from the entire nucleus, resulting in an enhancement to the photon spectrum over a broad energy range which is proportional to Z^2 (e.g., atomic number Z = 82 for Pb).

As a result, the rates for EM interactions (which include photon-photon and photon-nucleus scattering) are large enough to be measurable in Pb+Pb collisions at the LHC. Such collisions are commonly referred to as "ultra-peripheral collisions" (UPCs) because they can occur when the impact parameters between the incoming nuclei are large enough such that there is no hadronic interaction between the nuclei. ATLAS has measured UPC events where the basic interactions are photon-photon collisions [3–6], including light-by-light scattering and scattering where two leptons in the final state are produced. ATLAS has also measured UPC photo-nuclear collisions, for example in the case of dijet production [7]. In the photo-nuclear case, the photon could act as a point-like particle interacting with a parton in the nucleus (the 'direct' case). However, the vector-meson dominance picture suggests that the photon could fluctuate to a vector meson, for example a ρ meson, which then interacts with the Pb nucleus (the 'resolved' case) [1, 8]. Therefore, some subset of these collisions could be considered as ρ+nucleus collisions, albeit at a lower center-of-mass collision energy, depending on the ρ energy. Hence, such events will have an overall rapidity boost of the center-of-mass frame in the direction of the nucleus. Figure 1 illustrates direct and resolved photonuclear interactions.

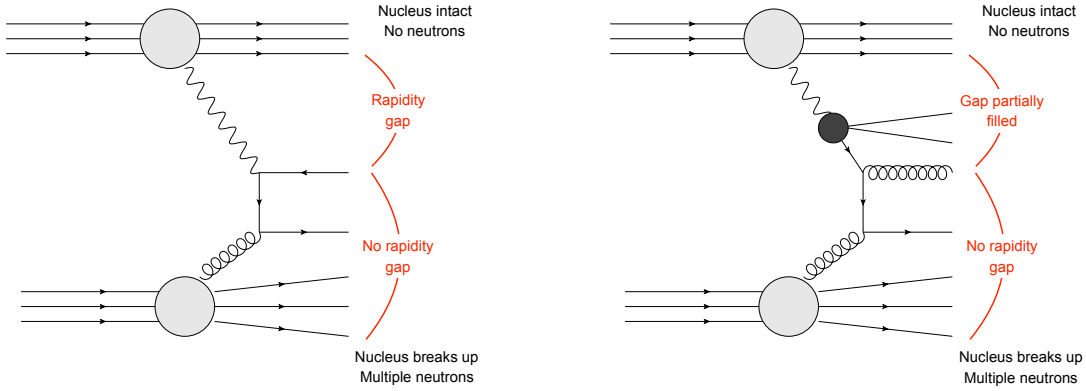

Figure 1: Shown are the diagrams representing different types of photo-nuclear collisions and the general features of their event topologies. Figure reproduced from Ref. [9].

Two-particle azimuthal correlations have been measured in such photo-nuclear events by ATLAS [9]. These results indicate significant non-zero elliptic and triangular flow coefficients, i.e., v_2 and v_3, respectively. These coefficients have been interpreted in terms of a hydrodynamically flowing medium [10], and alternatively in terms of scattering diagrams in the glasma framework [11]. The v_2 values are significantly smaller in UPC events compared with p+Pb events at the same particle multiplicity $N_{\mathrm{ch}}^{\mathrm{rec}}$. The lower elliptic flow in UPC events may be explained via longitudinal decorrelations in the rapidity-shifted UPC events in hydrodynamic calculations [10]. In Ref. [10], the authors make the specific prediction that the radial flow [12] is essentially the same in UPC and p+Pb collisions, as measured via the mean p_{T} of charged and identified particles. Other QGP signals observed in heavy-ion collisions such as baryon/meson enhancement [13] and strangeness enhancement [14], should also be quantified in these photo-nuclear collisions.

Thus, the analysis presented here is motivated by two central physics questions: (1) Can the underlying physics processes in UPC events be well modeled? and (2) Is there strong evidence for the formation of small quark-gluon plasma droplets that flow hydrodynamically in these UPC events? The analysis of charged-hadron yields in this note begins to address whether there is radial flow of the fluid as quantified by the p_{T} distributions. In the future, this analysis will be extended to the measurement of identified-hadron yields, which have additional sensitivity to the radial flow due to their higher mass. Furthermore, it will include the measurement of strangeness enhancement, and baryon/meson enhancement.

The analysis of photo-nuclear events detailed here thus utilizes the same 2018 Pb+Pb 5.02 TeV data set with an integrated luminosity of 1.73 nb^{-1} and comparable event selection cuts as the photo-nuclear flow analysis [9]. The 2015 p+Pb 5.02 TeV data set with an integrated luminosity of 0.10 nb^{-1} is also utilized for comparison purposes.

In this analysis, the inclusive yields of primary charged hadrons are quantified over the pseudorapidity (η) range $-2.5 < \eta < +2.5$[1] and as a function of transverse momentum (p_{T}). Primary particles are defined as

[1] ATLAS uses a right-handed coordinate system with its origin at the nominal interaction point (IP) in the centre of the detector and the z-axis along the beam pipe. The x-axis points from the IP to the centre of the LHC ring, and the y-axis points upwards. Cylindrical coordinates (r, Φ) are used in the transverse plane, Φ being the azimuthal angle around the z-axis. The pseudorapidity is defined in terms of the polar angle θ as $\eta = -\ln\tan(\theta/2)$. Angular distance is measured in units of $\Delta R \equiv \sqrt{(\Delta\eta)^2 + (\Delta\Phi)^2}$.

charged particles with a mean lifetime $\tau > 300$ ps (3×10^{-10} s), either directly produced in the collision or from subsequent decays of directly produced particles with $\tau < 30$ ps. This definition is consistent with previous ATLAS publications – see for example Ref. [15]. The per event yields of these charged hadrons are measured as a function of η and p_{T}, and as a function of UPC event class characterized by the charged particle multiplicity $N_{\mathrm{ch}}^{\mathrm{rec}}$. Detailed comparisons of these measurements with the Monte Carlo model DPMJET-III [16, 17] enables key constraints on the physics processes. Detailed comparisons between Pb+Pb UPC and p+Pb data enable tests of the hydrodynamical model predictions [10].

2 ATLAS detector

The ATLAS detector [18] at the LHC [19] covers nearly the entire solid angle around the collision point. It consists of an inner tracking detector surrounded by a thin superconducting solenoid, electromagnetic and hadronic calorimeters, and a muon spectrometer incorporating three large superconducting magnets. The inner-detector system (ID) is immersed in a 2 T axial magnetic field and provides charged-particle tracking in the range $|\eta| < 2.5$.

The high-granularity silicon pixel detector (Pix) covers the vertex region and typically provides three measurements per track. An inner–most insertable B-layer [20] has been operating as a part of the silicon pixel detector since 2015. It is followed by the silicon microstrip tracker (SCT) which usually provides four two-dimensional measurement points per track. These silicon detectors are complemented by the transition radiation tracker (TRT), which enables radially extended track reconstruction up to $|\eta| = 2.0$.

The calorimeter system covers the pseudorapidity range $|\eta| < 4.9$. Within the region $|\eta| < 3.2$, electromagnetic calorimetry is provided by barrel and endcap high-granularity lead/liquid-argon (LAr) electromagnetic calorimeters, with an additional thin LAr presampler covering $|\eta| < 1.8$, to correct for energy loss in material upstream of the calorimeters. Hadronic calorimetry is provided by the steel/scintillating-tile calorimeter, segmented into three barrel structures within $|\eta| < 1.7$, and two copper/LAr hadronic endcap calorimeters. The angular coverage is completed with forward copper/LAr and tungsten/LAr calorimeter modules optimised for electromagnetic and hadronic measurements respectively. The muon spectrometer (MS) surrounds the calorimeters and is based on three large air-core toroidal superconducting magnets with eight coils each. The MS includes a system of precision tracking chambers and fast detectors for triggering. The minimum-bias trigger scintillator (MBTS), reconfigured for Run 2, detects charged particles over $2.07 < |\eta| < 3.86$ using two hodoscopes of 12 counters positioned at $z = \pm 3.6$ m. The Zero-Degree Calorimeters (ZDCs) play a key role in identifying UPC events in heavy-ion collisions. They are located at $z = \pm 140$ m from the interaction point, just beyond the point where the common straight-section vacuum-pipe divides back into two independent beam-pipes. The ZDC modules consist of layers of alternating quartz rods and tungsten plates that measure neutral particles at pseudorapidities $|\eta| > 8.3$.

A two-level trigger system [21] is used to select events. The first-level trigger (L1) is implemented in hardware and uses a subset of the detector information to reduce the accepted rate to at most 100 kHz. This is followed by the software-based high level trigger (HLT) that reduced the accepted event rate to 1–4 kHz depending on the data-taking conditions during 2018 Pb+Pb collisions.

3 Data sample and event selection

The 2018 Pb+Pb $\sqrt{s_{NN}}$ = 5.02 TeV events were recorded with an integrated luminosity of 1.73 nb^{-1}, using a number of different triggers to sample high-multiplicity photo-nuclear collisions (γ+Pb). All triggers required one ZDC side to have a minimum amount of energy (E_{min} = 1 TeV) at L1 consistent with the presence of at least one spectator neutron (referred to as the Pb-going side and corresponding to $\eta < 0$), while the other side required an energy below E_{min}, consistent with no neutrons (referred to as the photon-going side and corresponding to $\eta > 0$). This topology is referred to as "`0nXn`" in this note. For the p+Pb data analysis, the 2016 p+Pb $\sqrt{s_{NN}}$ = 5.02 TeV data is used with an integrated luminosity of 0.10 nb^{-1} collected using a minimum bias trigger, as detailed in Ref. [22]. Monte Carlo events are run through GEANT4 [23, 24] and then the full event reconstruction.

The Monte Carlo simulation sample used in the Pb+Pb UPC analysis is a DPMJET-III + STARlight minimum bias γA collision sample. First, the distribution of photon flux for ^{208}Pb beams at the LHC was calculated using STARlight [25]. The flux distribution was passed to a multipurpose generator based on the Dual Parton Model (DPM) and referred to as DPMJET-III [16, 17], which simulates direct and resolved photon–lead (γ+Pb) interactions at the generator level. A PYTHIA γp collision sample is used for systematic uncertainty estimation. Both PYTHIA γp and DPMJET-III samples have their photon flux re-weighted to match that of STARlight. Peripheral HIJING [26] Pb+Pb collision events at 5.02 TeV are utilized for background modeling. The Monte Carlo sample that is used in p+Pb analysis is the HIJING p+Pb collision sample [27].

Each event is characterized by the number of reconstructed tracks with $p_{\text{T}} > 0.4$ GeV and $|\eta| < 2.5$, referred to as the reconstructed charged-particle multiplicity ($N_{\text{ch}}^{\text{rec}}$). This standard ATLAS event class definition utilizes reconstructed tracks that are not corrected for track acceptance and efficiency, see for example Refs. [28–31]. Monte Carlo studies indicate that selections on $N_{\text{ch}}^{\text{rec}}$ correspond to equivalent selections on truth-level charged particles also with $p_{\text{T}} > 0.4$ GeV and $|\eta| < 2.5$, but with $N_{\text{ch}}^{\text{truth}} \approx 1.2 \times N_{\text{ch}}^{\text{rec}}$.

There is one important event selection difference from [9] in that the measurement of charged-particle yields is auto-correlated with the event classification $N_{\text{ch}}^{\text{rec}}$, that is, a single track can enter both the yield and $N_{\text{ch}}^{\text{rec}}$. To avoid this auto-correlation, the azimuthal space is divided into separate regions: ε_ϕ for measuring the particle yield and (1-ε_ϕ) for measuring $N_{\text{ch}}^{\text{rec}}$, where ε_ϕ is the fraction of the total 2π azimuthal space. In the limit of $\varepsilon_\phi \to 0$, the standard $N_{\text{ch}}^{\text{rec}}$ definition is recovered. Different ε_ϕ regions of azimuthal space can be treated as separate events and the full statistics for the yield can be utilized. The default UPC Pb+Pb and p+Pb analyses use $\varepsilon_\phi = 0.01$, and a variation of $\varepsilon_\phi = 0.02$ is utilized for estimating the systematic uncertainty on this procedure.

In Pb+Pb UPC events, a reconstructed pseudorapidity gap quantity is used to distinguish between physics processes such as photo-nuclear collisions, low activity (peripheral) hadronic Pb+Pb collisions, and dissociative $\gamma\gamma \to X$ processes [32]. The requirement of a pseudorapidity gap above a minimum value in the photon-going direction is used to suppress contributions from hadronic peripheral Pb+Pb collisions. The gap quantities are constructed using tracks with $p_{\text{T}} > 0.4$ GeV , $|\eta| < 2.5$ and calorimeter clusters with $p_{\text{T}} > 0.2$ GeV , $|\eta| < 4.9$ in each event. The sum of gap quantity calculated in the photon-going half of the detector, $\sum_\gamma \Delta\eta^{\text{rec}}$ was originally introduced in Ref. [33] as a way to retain a large selection efficiency for resolved photon events which may break up a large gap with a photon fragment localized in pseudorapidity. The tracks and clusters at $\eta > 0$ are ordered in η, and then the two-particle pseudorapidity separations between adjacent particles $\Delta\eta$ are summed if they exceed 0.5. UPC events with $\sum_\gamma \Delta\eta^{\text{rec}} > 2.5$ are utilized in this analysis following the procedure in Ref. [9].

As with $N_{\mathrm{ch}}^{\mathrm{rec}}$, $\sum_{\gamma} \Delta\eta^{\mathrm{rec}}$ is defined in terms of reconstructed tracks and clusters and is not unfolded back to a truth level $\sum_{\gamma} \Delta\eta^{\mathrm{truth}}$ quantity. Monte Carlo generator studies utilizing PYTHIA γp, that match the $\sum_{\gamma} \Delta\eta^{\mathrm{rec}}$ distribution in Pb+Pb UPC data [9], indicate that a truth level $\sum_{\gamma} \Delta\eta^{\mathrm{truth}}$ selection with $p_{\mathrm{T}} > 0.45$ GeV and $|\eta| < 4.9$ reproduce the yield results with the reconstructed level $\sum_{\gamma} \Delta\eta^{\mathrm{rec}}$ selection, except at forward rapidity and high p_{T} where an additional < 5% systematic uncertainty is assigned to the experimental result.

In Pb+Pb UPC, to address the remaining contamination from Pb+Pb peripheral inelastic collisions despite the `0nXn` ZDC and $\sum_{\gamma} \Delta\eta^{\mathrm{rec}}$ selections, a purity correction factor, defined as the ratio of "true" UPC yield to measured UPC yield, is applied to the charged particle yields. To determine this correction factor, DPMJET-III and HIJING samples are utilized for the purity estimate, and p+Pb data for the contamination yield. The purity correction factor is about < 1-3% for yields in the photon-going direction and < 1% in the Pb-going direction.

Figure 2 (left) shows the Pb+Pb UPC $N_{\mathrm{ch}}^{\mathrm{rec}}$ distribution, including the additional selection on $\sum_{\gamma} \Delta\eta^{\mathrm{rec}}$ > 2.5. Figure 2 (right) shows the p+Pb minimum-bias $N_{\mathrm{ch}}^{\mathrm{rec}}$ distribution. The multiplicity range utilized in this analysis, $25 < N_{\mathrm{ch}}^{\mathrm{rec}} \leq 60$, is highlighted in both panels. Events with lower multiplicity ($N_{\mathrm{ch}}^{\mathrm{rec}} < 25$) are excluded as Pb+Pb UPC as there are important contributions from photo-diffractive and $\gamma\gamma \rightarrow q\bar{q}$ processes, as well as the desired photo-nuclear process. Additionally, the impurity estimates are less uncertain in this low multiplicity region and current Monte Carlo samples do not yield a good modeling of the $N_{\mathrm{ch}}^{\mathrm{rec}}$ and $\sum_{\gamma} \Delta\eta^{\mathrm{rec}}$ distribution. Events with higher multiplicity ($N_{\mathrm{ch}}^{\mathrm{rec}} > 60$) are excluded as there are very few Pb+Pb UPC events.

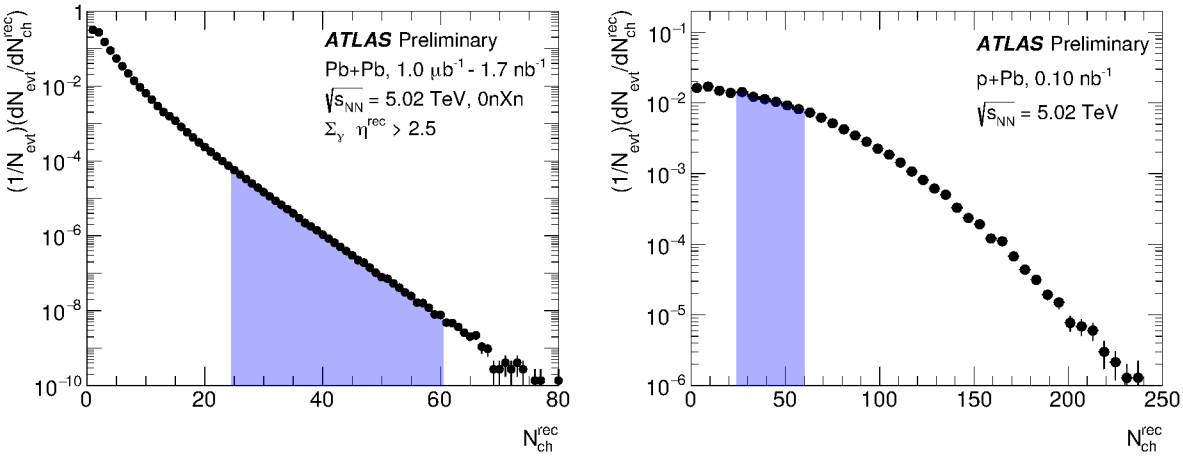

Figure 2: Shown is the multiplicity distribution ($N_{\mathrm{ch}}^{\mathrm{rec}}$) from Pb+Pb UPC (left) and p+Pb (right) collisions. The $N_{\mathrm{ch}}^{\mathrm{rec}}$ range, $25 < N_{\mathrm{ch}}^{\mathrm{rec}} \leq 60$, utilized in this analysis is highlighted.

The Pb+Pb UPC $N_{\mathrm{ch}}^{\mathrm{rec}}$ distribution falls more steeply than the p+Pb $N_{\mathrm{ch}}^{\mathrm{rec}}$ distribution. Thus, for comparing Pb+Pb UPC and p+Pb collisions, the p+Pb events are re-weighted in the $N_{\mathrm{ch}}^{\mathrm{rec}}$ interval of interest to match the Pb+Pb UPC $N_{\mathrm{ch}}^{\mathrm{rec}}$ distribution.

4 Analysis

This analysis reports charged hadron yields constructed using tracks detected in inner tracker originating from the collision. Primary particles are defined as charged particles with a mean lifetime $\tau > 300$ ps (3×10^{-10} s), either directly produced in the collision or from subsequent decays of directly produced particles with $\tau < 30$ ps. This definition is consistent with that used in the ATLAS publication [15]. To be explicit, this definition thus excludes particles with 3×10^{-11} s $< \tau < 3 \times 10^{-10}$ s, mainly strange baryons that have a very small probability to actually transverse the tracker before decaying (for example the Ξ^- with $\tau = 1.6 \times 10^{-10}$ s and Ω^- with $\tau = 0.8 \times 10^{-10}$ s). However, it includes charged hadrons resulting from the decay of, for example, Δ resonances and ρ mesons that have lifetimes shorter than 30 ps. The charged-particle track reconstruction follows those utilized for pp data-taking [15, 34]. Reconstructed charged-particle tracks are used in this analysis if they satisfy quality criteria as outlined in Ref. [35]. Tracks are further required to have $p_{\mathrm{T}} > 0.1$ GeV, $|\eta| < 2.5$, and a distance of closest approach to the reconstructed vertex in the longitudinal direction, and the transverse impact parameter, of less than 1.5 mm.

Charged-hadron yields are hence calculated as a function of p_{T} in different η slices:

$$Y(\eta, p_{\mathrm{T}}) = \frac{1}{N_{\mathrm{ev}}} \frac{\mathrm{d}N_{\mathrm{ch}}^2}{\mathrm{d}p_{\mathrm{T}}\mathrm{d}\eta} \tag{1}$$

and also integrated over p_{T} as a function of η:

$$Y(\eta) = \frac{1}{N_{\mathrm{ev}}} \frac{\mathrm{d}N_{\mathrm{ch}}}{\mathrm{d}\eta}, \tag{2}$$

where N_{ev} is the number of selected events and N_{ch} is the number of charged particles. The charged-particle yield is corrected for reconstruction and selection inefficiency, as well as for contributions from tracks which are not associated with primary particles, on a per-track basis using simulation-derived correction factors. The yields as a function of η are measured for $p_{\mathrm{T}} > 0.1$ GeV and extrapolated via the DPMJET-III Monte Carlo sample down to $p_{\mathrm{T}} = 0$ GeV. The systematic uncertainty on this extrapolation is $< 3\%$.

Finally, using the yields detailed above, the $\langle\eta\rangle$ within the measured region $|\eta| < 2.5$ and the $\langle p_{\mathrm{T}}\rangle$ in η intervals are calculated as a function of event classification $N_{\mathrm{ch}}^{\mathrm{rec}}$. These mean values are calculated after extrapolating down to $p_{\mathrm{T}} = 0$ GeV.

The reconstruction efficiency is defined as the ratio of the number of truth primary charged particles whose associated reconstructed track has a truth-matched primary charged particle $N_{\mathrm{truth}}^{\mathrm{matched}}$ (as defined in Ref. [36]) to the total number of truth primary charged particles, N_{truth}, as a function of both p_{T} and η:

$$\varepsilon(p_{\mathrm{T}}, \eta) = \frac{N_{\mathrm{truth}}^{\mathrm{matched}}(p_{\mathrm{T}}, \eta)}{N_{\mathrm{truth}}(p_{\mathrm{T}}, \eta)} \tag{3}$$

In the analysis of the Pb+Pb UPC data, separate corrections are defined for events in which the photon is going in the positive or negative direction along z-axis and are applied accordingly.

The reconstruction efficiency as a function of p_{T} is fitted using a polynomial function of 5^{th} order in $\log(p_{\mathrm{T}})$ at low p_{T} ($p_{\mathrm{T}} < 1$ GeV) and a polynomial function of 1^{st} order in $\log(p_{\mathrm{T}})$ at high p_{T} ($p_{\mathrm{T}} > 1$ GeV) in each of the 25 η bins spanning from -2.5 to 2.5. The two fit functions are made continuous at the intersection p_{T} = 1 GeV.

Background tracks consist of fake tracks and secondary tracks. Fake tracks are defined as tracks that do not have a truth primary match. The largest sources of secondary tracks are from hadronic interactions of particles with the detector material and the decay products of particles with strange quark content, mostly K^0 and Λ^0 decays. Additionally, photon conversions, specifically below 0.5 GeV, also contribute significantly to the production of secondary tracks. In order to correct for the fakes and secondary contributions, tracks are weighted on a track-by-track basis by "primary fraction", f_{primary}, which is estimated as a function of reconstructed kinematics in simulated events by taking the ratio of the number of primary tracks $N_{\text{ch}}^{\text{primary}}$ to the number of reconstructed tracks N_{ch}:

$$f_{\text{primary}}(p_{\text{T}}, \eta) = \frac{N_{\text{ch}}^{\text{primary}}(p_{\text{T}}, \eta)}{N_{\text{ch}}(p_{\text{T}}, \eta)} \tag{4}$$

The sources of systematic uncertainty in this measurement are discussed below. There are uncertainties assigned to the purity estimation of photo-nuclear events, and to the comparison of results using only events where the photon is headed along the positive-z direction of the detector with those where it is headed towards the negative-z direction [9]. There are uncertainties assigned to the track selection, fakes and secondary tracks, and the mis-modeling of the detector material [15, 37]. To quantify the uncertainty on extrapolation to $p_{\text{T}} = 0$ GeV, variations obtained from the fits to the p_{T} distribution are utilized. There is a subdominant uncertainty associated with the use of $\sum_{\gamma} \Delta\eta$ at the reconstruction level compared to truth level. Furthermore, uncertainty on the fit values of track reconstruction efficiency are accounted for. An uncertainty is also assigned addressing the lack of correction for bin migration due to track momentum resolution.

The uncertainties are typically evaluated by repeating the full analysis chain with a given systematic variation, which may result in, e.g., a different reconstructed-level distribution. To have statistically-independent samples between the nominal and the variations, in all relevant cases, the data samples are divided randomly into two subsets: one half of the events are used for the nominal condition, the other half events are used for the variation. The ratio of the varied to nominal result is fitted using a function, and the fitted values are assigned as the systematic uncertainty. All uncertainties contributions are added in quadrature for the full systematic uncertainty.

The dominant sources of systematic uncertainty for $Y(\eta, p_{\text{T}})$ in Pb+Pb UPC are from event purity, lack of correction for bin migration due to track momentum resolution and truth gap definition in the p_{T} region > 0.4 GeV, all comparable to each other, within 4%. In p+Pb , the dominant sources of uncertainty are mis-modeling of the detector material and track bin migration in the p_{T} region > 0.4 GeV region, about 2%. In the lowest p_{T} region 0.1-0.4 GeV, the dominant sources of uncertainties are from mis-modeling of the detector material, within 5%. The main sources of systematic uncertainty for $Y(\eta)$ at mid-rapidity arise from extrapolation to $p_{\text{T}} > 0$ GeV, fakes and secondaries, and mis-modeling of the detector material, all at a level of approximately 2%. In the most forward/backward rapidity bins, the dominant source of systematic uncertainty is from material variations, within 3%.

5 Results

The charged-hadron yields are presented in 5.02 TeV Pb+Pb UPC and p+Pb collisions both (i) as a function of p_{T} in six exclusive intervals of η and (ii) integrated over all p_{T} as a function of η. The yields are first shown for the $N_{\mathrm{ch}}^{\mathrm{rec}}$ selection, $25 < N_{\mathrm{ch}}^{\mathrm{rec}} \leq 60$, where the p+Pb events are re-weighted to have effectively the same $N_{\mathrm{ch}}^{\mathrm{rec}}$ distribution as the UPC Pb+Pb events. Additionally, the distribution in p+Pb is re-weighted to have the same integral of $\mathrm{d}N_{\mathrm{ch}}/\mathrm{d}\eta$ in Pb+Pb UPC over the η range, -2.5 to 2.5. Negative η corresponds to Pb-going direction, and positive η corresponds to the photon-going and proton-going directions in Pb+Pb UPC and p+Pb , respectively.

Figure 3 shows the charged-hadron yields as a function of p_{T} in six η selections: [-2.5,-1.6], [-1.6,-0.8], [-0.8,0.0], [0,0.8], [0.8,1.6], [1.6,2.5]. The left panel shows Pb+Pb UPC results and the right panel shows p+Pb results.

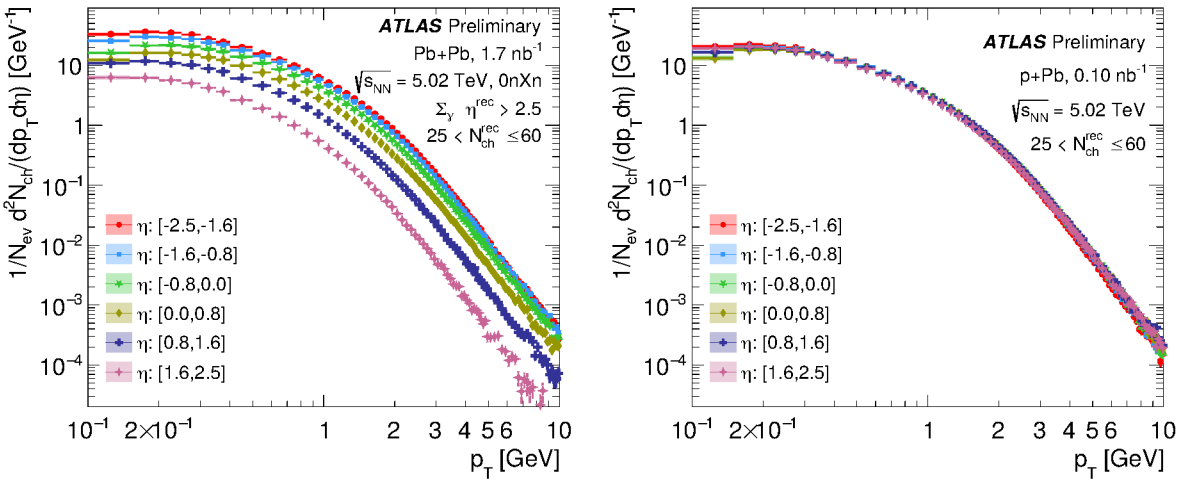

Figure 3: Shown are the charged-hadron yields as a function of p_{T} in six η selections. The left panel is for UPC Pb+Pb collisions and the right panel for p+Pb collisions. Statistical uncertainties are shown as vertical lines and systematic uncertainties are shown as open boxes. For most points the systematic uncertainties are smaller than the markers.

Figure 4 shows the charged-hadron yields as a function of η for Pb+Pb UPC and p+Pb , for $p_{\mathrm{T}} > 0$ GeV. The Pb+Pb UPC distribution is highly asymmetric, as expected given the lower energy of the photon compared with the energy per nucleon in the opposing Pb nucleus. In contrast, the p+Pb distribution is nearly symmetric. In central p+Pb collisions the distribution is asymmetric [38]. However, in this analysis, low multiplicity p+Pb events are selected, and hence the η distribution is more pp like.

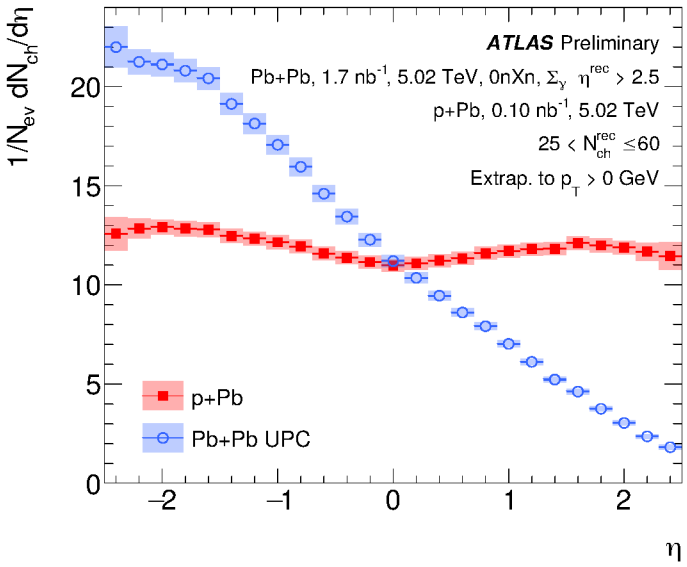

Figure 4: Shown are the charged-hadron yields as a function of η extrapolated to $p_{\mathrm{T}} > 0$ GeV for Pb+Pb UPC and p+Pb collisions. The statistical uncertainties are shown as vertical lines and systematic uncertainties are shown as open boxes.

In order to examine charged-hadron production more differentially in Pb+Pb UPC, the experimental data is split into several $\Delta N_{\mathrm{ch}}^{\mathrm{rec}} = 5$ wide categories. Figure 5 shows $\mathrm{d}N_{\mathrm{ch}}/\mathrm{d}\eta$ for seven categories in $N_{\mathrm{ch}}^{\mathrm{rec}}$ for $p_{\mathrm{T}} >$ 0 GeV. The average charged-hadron pseudorapidity within the region of the measurement $-2.5 < \eta < +2.5$ is quantified for each $N_{\mathrm{ch}}^{\mathrm{rec}}$ selection in data. Figure 6 shows $\langle\eta\rangle$ as a function of $N_{\mathrm{ch}}^{\mathrm{rec}}$ utilizing the yields for $p_{\mathrm{T}} > 0$ GeV.

One can also examine the p_{T} distributions in these finer $N_{\mathrm{ch}}^{\mathrm{rec}}$ selections. Figure 7 shows $\langle p_{\mathrm{T}}\rangle$ for p_{T} > 0 GeV as a function of $N_{\mathrm{ch}}^{\mathrm{rec}}$ in two η regions, [-1.6,-0.8] and [0.8,1.6], in Pb+Pb UPC and p+Pb collisions. At negative η, $\langle p_{\mathrm{T}}\rangle$ between the two collision systems is comparable and in agreement for $N_{\mathrm{ch}}^{\mathrm{rec}} > 30$. In contrast, on the photon-going side ($\eta > 0$), there is a large difference in the $\langle p_{\mathrm{T}}\rangle$ between the two collision systems for all $N_{\mathrm{ch}}^{\mathrm{rec}}$. This observation is consistent with the difference in the shape of the p_{T} distributions between Pb+Pb UPC and p+Pb in the η selections of interest. The substantially larger $\langle p_{\mathrm{T}}\rangle$ at negative η in Pb+Pb UPC, and it's comparable magnitude in p+Pb , may already hint at a contribution from radial flow discussed earlier. Further tests measuring the $\langle p_{\mathrm{T}}\rangle$ of identified hadrons are needed to confirm this hypothesis.

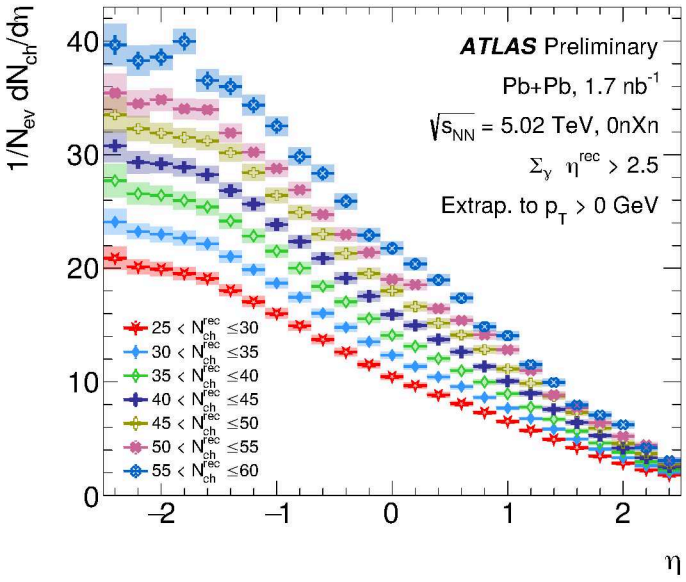

Figure 5: Shown are the charged-hadron yields as a function of η in different $N_{\mathrm{ch}}^{\mathrm{rec}}$ bins in Pb+Pb UPC collisions extrapolated to $p_{\mathrm{T}} > 0$ GeV. Vertical lines are statistical uncertainties and shaded boxes are systematic uncertainties.

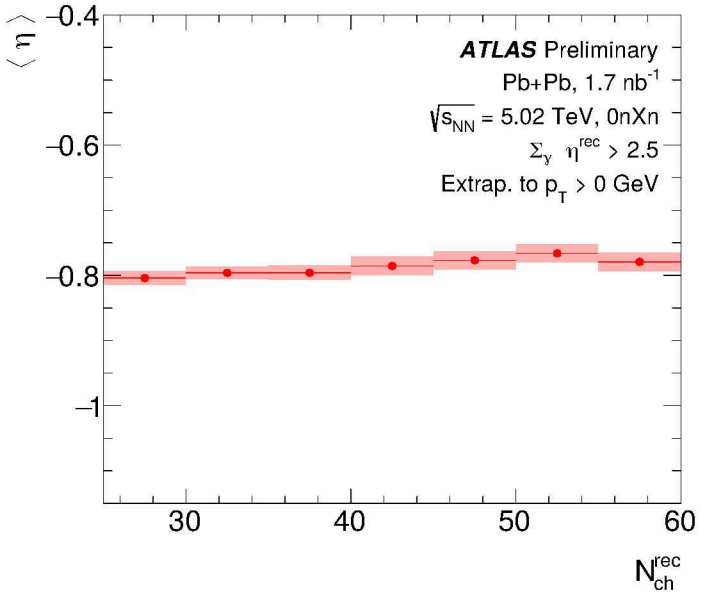

Figure 6: Shown are the calculated $\langle\eta\rangle$ values within the window $-2.5 < \eta < +2.5$ of charged-hadron yields as a function of $N_{\mathrm{ch}}^{\mathrm{rec}}$ in Pb+Pb UPC collisions. The charged-hadron yields are extrapolated to $p_{\mathrm{T}} > 0$ GeV. Vertical lines, often smaller than the markers, are statistical uncertainties and shaded boxes are systematic uncertainties.

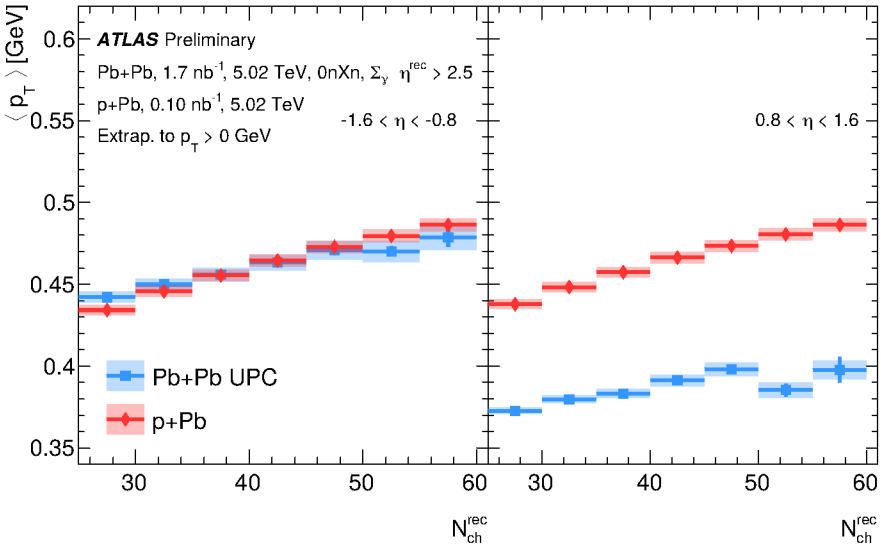

Figure 7: Shown are the $\langle p_{\mathrm{T}} \rangle$ of charged-hadron yields as a function of $N_{\mathrm{ch}}^{\mathrm{rec}}$ in Pb+Pb UPC collisions and p+Pb collisions in two different η slices, [-1.6,-0.8] (left) and [0.8,1.6] (right). The charged-hadron yields are extrapolated to $p_{\mathrm{T}} > 0$ GeV. Vertical lines, often smaller than the markers, are statistical uncertainties and shaded boxes are systematic uncertainties.

6 Monte Carlo DPMJET-III comparisons

In order to further examine the relationship between particle production and photon energy, Figure 8 (left) shows the photon energy distribution in the DPMJET-III model with different $N_{\mathrm{ch}}^{\mathrm{rec}}$ selections. A very large number of events have extremely low E_γ (E_γ < 10 GeV) for the lowest $N_{\mathrm{ch}}^{\mathrm{rec}}$ selection (which is below the range used in this analysis). Figure 8 (right) shows the correlation between photon energy and $N_{\mathrm{ch}}^{\mathrm{rec}}$ in DPMJET-III events. Events with larger $N_{\mathrm{ch}}^{\mathrm{rec}}$ select cases where the emitted photon has larger energy. The figure also presents $W_{\gamma A}$, the effective center-of-mass energy of the photon-nucleus system (per nucleon), in a secondary axis to highlight the energy-dependence of the multiplicities.

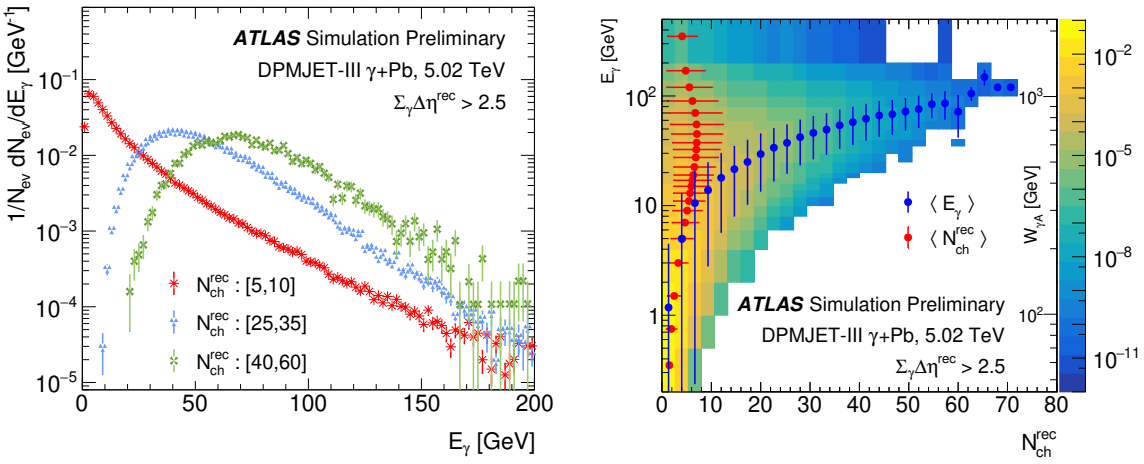

Figure 8: (left) Truth photon energy distribution from the Monte Carlo model DPMJET-III. The DPMJET-III results are shown with three selections on $N_{\mathrm{ch}}^{\mathrm{rec}}$. (right) Correlation between photon energy and $N_{\mathrm{ch}}^{\mathrm{rec}}$ in DPMJET-III. The blue points represent the mean photon energy value in each $N_{\mathrm{ch}}^{\mathrm{rec}}$ bin and the red points represent the mean $N_{\mathrm{ch}}^{\mathrm{rec}}$ in each E_γ bin. The vertical/horizontal error bars represent the standard deviation. Additionally, $W_{\gamma A}$ is presented in the right y-axis.

DPMJET-III events run through the full ATLAS GEANT4 [23, 24] and reconstruction chain can be directly compared with data. Figures 9 and 10 show the DPMJET-III truth-level yield results compared to the experimental results in Pb+Pb UPC for $25 < N_{\mathrm{ch}}^{\mathrm{rec}} \leq 60$ as a function of η and p_{T}, respectively. Notably, the DPMJET-III event selection is at the reconstructed level, i.e., $N_{\mathrm{ch}}^{\mathrm{rec}}$ and $\sum_\gamma \Delta\eta^{\mathrm{rec}}$, to match the experimental event selection. The DPMJET-III results also used the ε_ϕ method detailed above to remove the auto-correlation between the yield and $N_{\mathrm{ch}}^{\mathrm{rec}}$. DPMJET-III over-predicts the yield at forward rapidity, though with a reasonable description of the steeply falling p_{T} distribution. At backward rapidity, DPMJET-III slightly under-predicts the yield and with a significant underestimate of the high p_{T} yields.

Examining the comparison more differentially in $N_{\mathrm{ch}}^{\mathrm{rec}}$, Figure 11 shows four specific $N_{\mathrm{ch}}^{\mathrm{rec}}$ bins with comparison to DPMJET-III generator level calculations. The $\mathrm{d}N_{\mathrm{ch}}/\mathrm{d}\eta$ distribution in DPMJET-III gives a reasonable description of the particle yield at backward rapidity, while consistently over-predicting the yield at forward rapidity in all $N_{\mathrm{ch}}^{\mathrm{rec}}$ selections.

Figure 12 shows $\langle\eta\rangle$ as a function of $N_{\mathrm{ch}}^{\mathrm{rec}}$ in both UPC data and DPMJET-III. A significant difference in $\langle\eta\rangle$ is observed between UPC data and DPMJET-III model at all $N_{\mathrm{ch}}^{\mathrm{rec}}$. The DPMJET-III over-prediction of the yield at forward-rapidity leads to a $\langle\eta\rangle$ closer to zero that seen in data. Figure 13 shows the calculated $\langle p_{\mathrm{T}}\rangle$ extrapolated for $p_{\mathrm{T}} > 0$ GeV as a function of $N_{\mathrm{ch}}^{\mathrm{rec}}$ in two η selections, [-1.6,-0.8] and [0.8,1.6], in

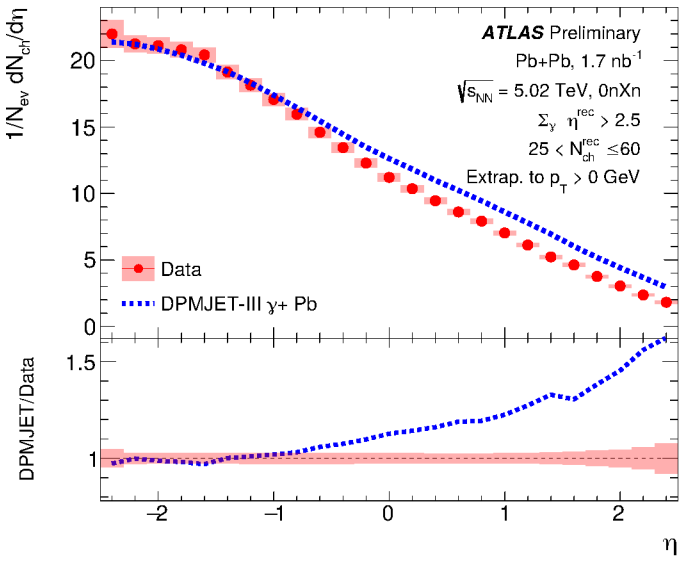

Figure 9: Shown are the charged-hadron yields as a function of η in Pb+Pb UPC data extrapolated to $p_{\mathrm{T}} > 0$ GeV. Also, shown are the truth-level yield result from reconstructed event generated by DPMJET-III utilizing the identical $N_{\mathrm{ch}}^{\mathrm{rec}}$ and $\sum_\gamma \Delta\eta^{\mathrm{rec}}$ selection criteria as with experimental data. The bottom panels show the ratio of DPMJET-III to data.

Pb+Pb UPC collisions. DPMJET-III provides a good description of the $\langle p_{\mathrm{T}} \rangle$ at forward rapidity, despite over-predicting the yield in this region, and significantly under-predicts the $\langle p_{\mathrm{T}} \rangle$ at backward rapidity, despite describing the yield in this region.

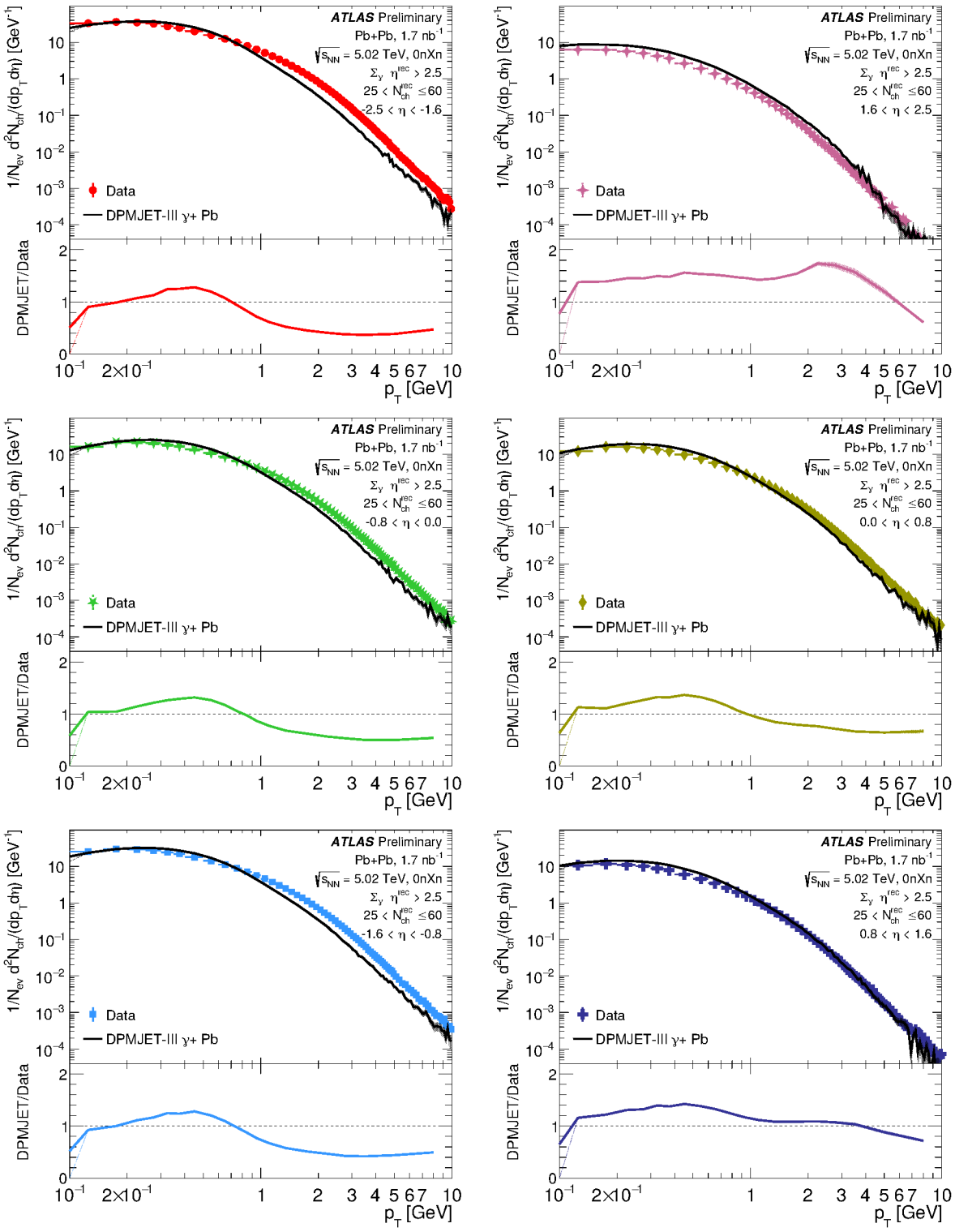

Figure 10: Shown are the charged-hadron yields as a function of p_{T} in three different η slices in Pb+Pb UPC data. Also, shown are the truth-level yield results from reconstructed event generated by DPMJET-III utilizing the identical $N_{\mathrm{ch}}^{\mathrm{rec}}$ and $\sum_{\gamma} \Delta\eta^{\mathrm{rec}}$ selection criteria as with experimental data. The bottom panels show the ratio of DPMJET-III γ+ Pb results to data.

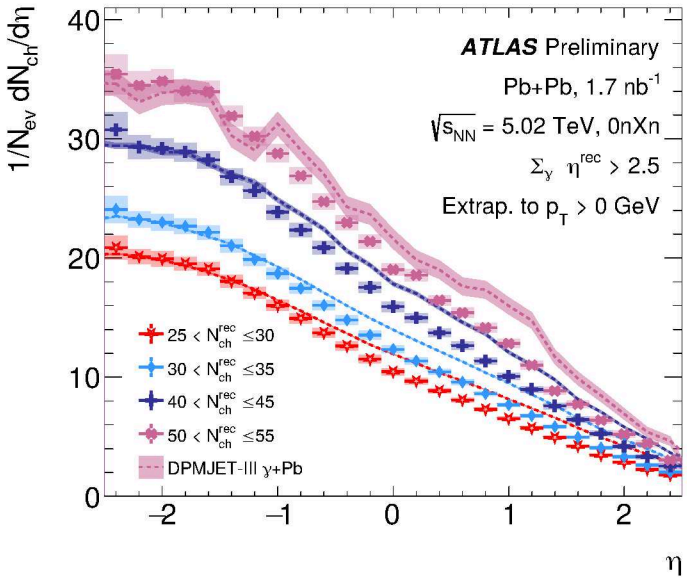

Figure 11: Shown are the charged-hadron yields as a function of η in different $N_{\mathrm{ch}}^{\mathrm{rec}}$ bins in Pb+Pb UPC collisions extrapolated to $p_{\mathrm{T}} > 0$ GeV. Vertical lines are statistical uncertainties and open boxes are systematic uncertainties. Also, shown are the truth-level yield results from reconstructed event generated by DPMJET-III utilizing the identical $N_{\mathrm{ch}}^{\mathrm{rec}}$ and $\sum_{\gamma} \Delta\eta^{\mathrm{rec}}$ selection criteria as with experimental data.

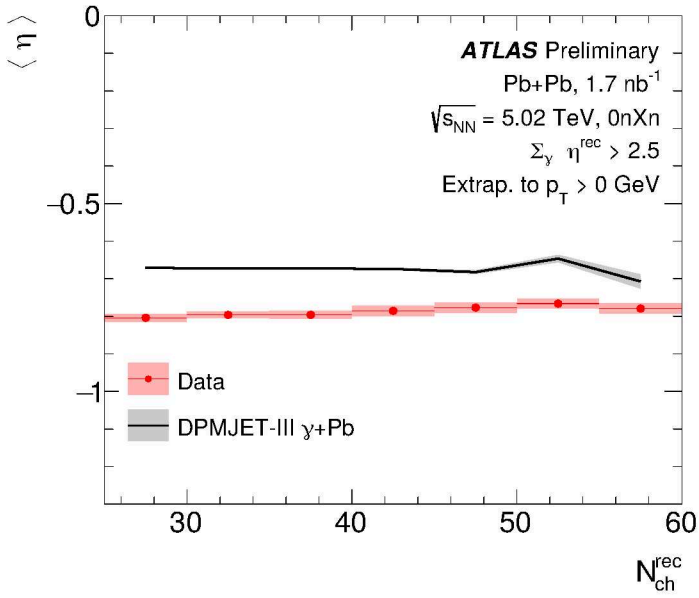

Figure 12: Shown are the calculated $\langle\eta\rangle$ values within the window $-2.5 < \eta < +2.5$ of charged-hadron yields as a function of $N_{\mathrm{ch}}^{\mathrm{rec}}$ in Pb+Pb UPC collisions. The charged-hadron yields are extrapolated to $p_{\mathrm{T}} > 0$ GeV. Also, shown are the truth-level yield result from reconstructed event generated by DPMJET-III utilizing the identical $N_{\mathrm{ch}}^{\mathrm{rec}}$ and $\sum_{\gamma} \Delta\eta^{\mathrm{rec}}$ selection criteria as with experimental data.

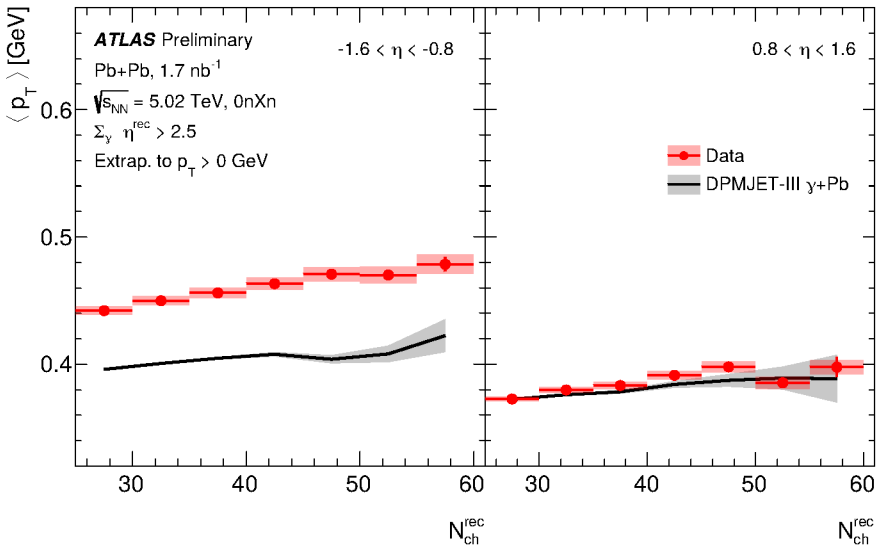

Figure 13: Shown are the $\langle p_{\mathrm{T}} \rangle$ of charged-hadron yields as a function of $N_{\mathrm{ch}}^{\mathrm{rec}}$ in Pb+Pb UPC collisions in two different η slices, [-1.6,-0.8] (left) and [0.8,1.6] (right). The charged-hadron yields are extrapolated to $p_{\mathrm{T}} > 0$ GeV. Also, shown are the truth-level yield result from reconstructed event generated by DPMJET-III utilizing the identical $N_{\mathrm{ch}}^{\mathrm{rec}}$ and $\sum_{\gamma} \Delta\eta^{\mathrm{rec}}$ selection criteria as with experimental data.

7 Conclusion

This note details the analysis of 5.02 TeV Pb+Pb UPC and p+Pb data taken by the ATLAS experiment at the LHC. Charged-hadron yields as a function of transverse momentum p_{T} and pseudorapidity η, and in selections in event multiplicity $N_{\mathrm{ch}}^{\mathrm{rec}}$, are quantified. Also, $\langle\eta\rangle$, the mean value of yields measured in $|\eta| < 2.5$, and $\langle p_{\mathrm{T}}\rangle$, the mean value of yields measured in η intervals, are measured within selections of $N_{\mathrm{ch}}^{\mathrm{rec}}$. Monte Carlo DPMJET-III does not describe the detailed charged-hadron distributions, notably the $\langle\eta\rangle$, having a larger yield at forward rapidity, and under-predicting the $\langle p_{\mathrm{T}}\rangle$ at backward rapidity. Constraints on these types of models are critical for accurate calculations of potential collective flow effects previously published by ATLAS [9]. In addition, other potential signatures of collectivity including radial expansion are tested in this analysis via the $\langle p_{\mathrm{T}}\rangle$ comparison in Pb+Pb UPC and p+Pb collisions. The larger $\langle p_{\mathrm{T}}\rangle$ at backward compared to forward rapidity in Pb+Pb UPC may hint at hydrodynamic radial flow.

Appendix

A Monte Carlo DPMJET-III discussion

A further study into the relationship between particle production and photon energy is detailed here. Figure 14 shows the DPMJET-III truth photon energy distribution for events with the generator level $\sum_{\gamma}\Delta\eta^{\mathrm{rec}} > 2.5$ selection and no selection on $N_{\mathrm{ch}}^{\mathrm{rec}}$. Additionally, two re-weightings of the photon energy distribution are shown, referred to as "higher" and "lower", that increase (decrease) the relative contribution of high-energy photons. These re-weightings are not motivated for example by expected uncertainties in the STARlight flux calculation and rather are selected as extremes just to test the impact on the $\langle\eta\rangle$ and $\langle p_{\mathrm{T}}\rangle$.

Any change in the photon energy distribution shifts the particle production in pseudorapidity. The typical UPC photon energy is lower than the individual nucleon energy in the opposing Pb nucleus, and hence the rapidity distribution is shifted towards the Pb-going direction, i.e., backward rapidity. However, for higher energy photons, one expects a smaller rapidity shift and hence the $\langle\eta\rangle$ value increases towards zero. The change in photon energy concordantly shifts the $\sum_{\gamma}\Delta\eta^{\mathrm{rec}}$ distribution too.

Figure 15 shows the $\sum_{\gamma}\Delta\eta^{\mathrm{rec}}$ distribution for $25 < N_{\mathrm{ch}}^{\mathrm{rec}} \leq 60$ (left) and $\langle\eta\rangle$ as a function of $N_{\mathrm{ch}}^{\mathrm{rec}}$ (right) for each of the three photon energy distributions. The distribution with more low-energy photons, shown by the green lines, yields $\sum_{\gamma}\Delta\eta^{\mathrm{rec}}$ distribution and $\langle\eta\rangle$ in closer agreement with data. Conversely, the distribution with more high-energy photons, shown by the magenta lines, yields $\sum_{\gamma}\Delta\eta^{\mathrm{rec}}$ distribution and $\langle\eta\rangle$ results in greater disagreement with Pb+Pb UPC data.

Figure 16 shows the $\langle p_{\mathrm{T}}\rangle$ as a function of $N_{\mathrm{ch}}^{\mathrm{rec}}$ for each of the three photon energy distributions. There is no significant difference between the $\langle p_{\mathrm{T}}\rangle$ obtained from nominal photon energy distribution compared to those obtained from re-weighted photon energy distribution.

The very substantial energy re-weighting applied to DPMJET-III that emphasizes lower energy photons, referred to as "lower", is quite likely ruled out by other Pb+Pb UPC measurements. It is notable that such a large change does naturally shift the $\langle\eta\rangle$ and $\sum_{\gamma}\Delta\eta^{\mathrm{rec}}$ distributions, while having a very modest impact on the $\langle p_{\mathrm{T}}\rangle$.

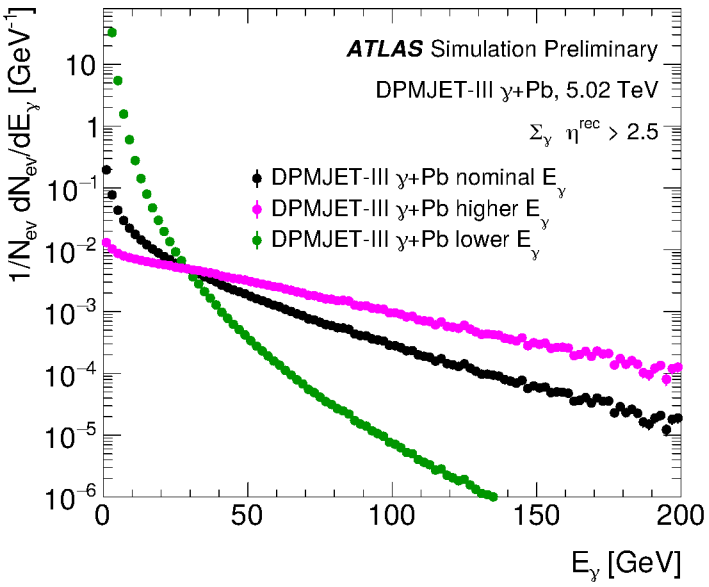

Figure 14: Shown are the DPMJET-III truth photon energy distribution for events with the generator level $\sum_\gamma \Delta\eta^{rec}$ > 2.5 selection and no selection on N_{ch}^{rec}. Additionally, two re-weightings of the photon energy distribution are shown, referred to as "higher" and "lower", that increase (decrease) the relative contribution of high-energy photons.

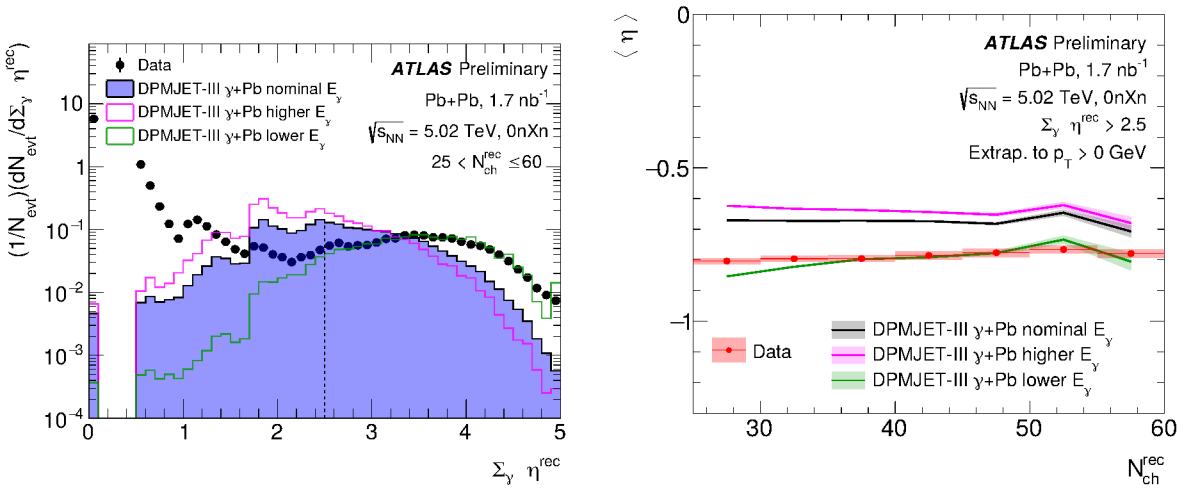

Figure 15: (left) Shown is the $\sum_\gamma \Delta\eta^{rec}$ distribution for data events corresponding to N_{ch}^{rec} = 25-60. Also, shown are the results from reconstructed event generated by DPMJET-III not corrected for detector effects utilizing the identical N_{ch}^{rec} and $\sum_\gamma \Delta\eta^{rec}$ selection criteria as with experimental data for the nominal DPMJET-III and the two variations in the photon energy distribution, i.e., "higher" and "lower". The black dashed line corresponds to the $\sum_\gamma \Delta\eta^{rec}$ selection cut. (right) Shown is the $\langle\eta\rangle$ as a function of N_{ch}^{rec} compared to the nominal truth-level yield result in DPMJET-III and two variations.

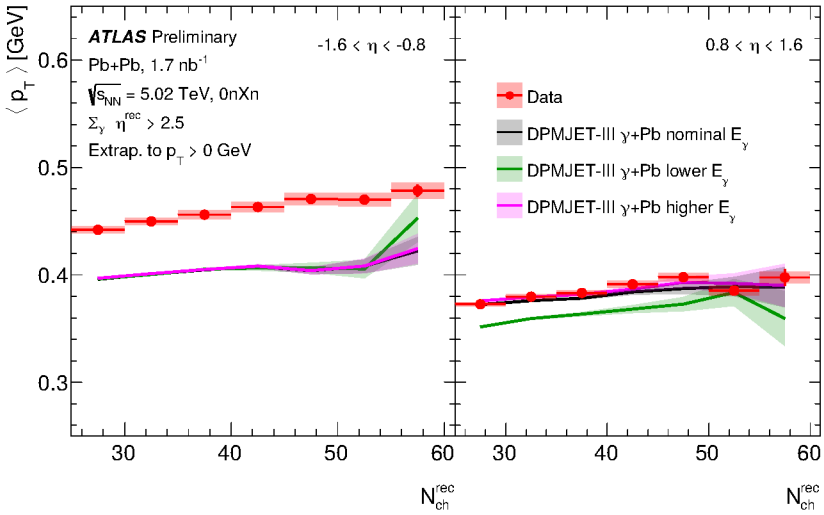

Figure 16: Shown are the $\langle p_{\mathrm{T}} \rangle$ as a function of $N_{\mathrm{ch}}^{\mathrm{rec}}$. The left panel shows the result for the backward rapidity slice [-1.6,-0.8] and the right panel shows the result for the forward rapidity slice [0.8,1.6] utilizing results extrapolated to $p_{\mathrm{T}} > 0$ GeV. Also, shown are the truth-level yield result from reconstructed event generated by DPMJET-III utilizing the identical $N_{\mathrm{ch}}^{\mathrm{rec}}$ and $\sum_{\gamma} \Delta\eta^{\mathrm{rec}}$ selection criteria as with experimental data for the nominal DPMJET-III and the two variations in the photon energy distribution, i.e., "higher" and "lower".

References

[1] C. A. Bertulani, S. R. Klein and J. Nystrand, *Physics of ultra-peripheral nuclear collisions*, Ann. Rev. Nucl. Part. Sci. **55** (2005) 271, arXiv: nucl-ex/0502005 (cit. on p. 2).

[2] S. R. Klein and H. Mäntysaari, *Imaging the nucleus with high-energy photons*, Nature Rev. Phys. **1** (2019) 662, arXiv: 1910.10858 [hep-ex] (cit. on p. 2).

[3] ATLAS Collaboration, *Measurement of high-mass dimuon pairs in ultra-peripheral lead–lead collisions at* $\sqrt{s_{NN}} = 5.02$ *TeV with the ATLAS detector at the LHC*, ATLAS-CONF-2016-025, 2016, URL: https://cds.cern.ch/record/2157689 (cit. on p. 2).

[4] ATLAS Collaboration, *Evidence for light-by-light scattering in heavy-ion collisions with the ATLAS detector at the LHC*, Nature Phys. **13** (2017) 852, arXiv: 1702.01625 [hep-ex] (cit. on p. 2).

[5] ATLAS Collaboration, *Observation of Light-by-Light Scattering in Ultraperipheral Pb+Pb Collisions with the ATLAS Detector*, Phys. Rev. Lett. **123** (2019) 052001, arXiv: 1904.03536 [hep-ex] (cit. on p. 2).

[6] ATLAS Collaboration, *Observation of the* $\gamma\gamma \to \tau\tau$ *process in Pb+Pb collisions and constraints on the* τ*-lepton anomalous magnetic moment with the ATLAS detector*, (2022), arXiv: 2204.13478 [hep-ex] (cit. on p. 2).

[7] ATLAS Collaboration, *Photo-nuclear dijet production in ultra-peripheral Pb+Pb collisions*, ATLAS-CONF-2017-011, 2017, URL: https://cds.cern.ch/record/2244822 (cit. on p. 2).

[8] A. Baltz et al., *The physics of ultraperipheral collisions at the LHC*, Physics Reports **458** (2008) 1 (cit. on p. 2).

[9] ATLAS Collaboration, *Two-particle azimuthal correlations in photonuclear ultraperipheral Pb+Pb collisions at 5.02 TeV with ATLAS*, Phys. Rev. C **104** (2021) 014903, arXiv: 2101.10771 [nucl-ex] (cit. on pp. 3, 5, 6, 8, 18).

[10] W. Zhao, C. Shen and B. Schenke, *Collectivity in Ultraperipheral Pb+Pb Collisions at the Large Hadron Collider*, Phys. Rev. Lett. **129** (2022) 252302, arXiv: 2203.06094 [nucl-th] (cit. on pp. 3, 4).

[11] Y. Shi, L. Wang, S.-Y. Wei, B.-W. Xiao and L. Zheng, *Exploring collective phenomena at the electron-ion collider*, Phys. Rev. D **103** (2021) 054017, arXiv: 2008.03569 [hep-ph] (cit. on p. 3).

[12] U. Heinz and R. Snellings, *Collective flow and viscosity in relativistic heavy-ion collisions*, Ann. Rev. Nucl. Part. Sci. **63** (2013) 123, arXiv: 1301.2826 [nucl-th] (cit. on p. 3).

[13] R. J. Fries, B. Müller, C. Nonaka and S. A. Bass, *Hadronization in Heavy-Ion Collisions: Recombination and Fragmentation of Partons*, Phys. Rev. Lett. **90** (20 2003) 202303, URL: https://link.aps.org/doi/10.1103/PhysRevLett.90.202303 (cit. on p. 3).

[14] ALICE Collaboration, *Enhanced production of multi-strange hadrons in high-multiplicity proton-proton collisions*, Nature Phys. **13** (2017) 535, arXiv: 1606.07424 [nucl-ex] (cit. on p. 3).

[15] ATLAS Collaboration, *Charged-particle multiplicities in pp interactions measured with the ATLAS detector at the LHC*, New J. Phys. **13** (2011) 053033, arXiv: 1012.5104 [hep-ex] (cit. on pp. 4, 7, 8).

[16] R. Engel,
Photoproduction within the two component Dual Parton Model: Amplitudes and cross sections,
Z. Phys. C **66** (1995) 203 (cit. on pp. 4, 5).

[17] S. Roesler, R. Engel and J. Ranft, 'The Monte Carlo Event Generator DPMJET-III',
International Conference on Advanced Monte Carlo for Radiation Physics, Particle Transport Simulation and Applications (MC 2000), 2000 1033, arXiv: hep-ph/0012252 (cit. on pp. 4, 5).

[18] ATLAS Collaboration, *The ATLAS Experiment at the CERN Large Hadron Collider*,
JINST **3** (2008) S08003 (cit. on p. 4).

[19] L. Evans and P. Bryant, *LHC Machine*, JINST **3** (2008) S08001 (cit. on p. 4).

[20] ATLAS Collaboration, *ATLAS Insertable B-Layer Technical Design Report*, ATLAS-TDR-19, 2010,
URL: https://cds.cern.ch/record/1291633,
ATLAS Insertable B-Layer Technical Design Report Addendum, ATLAS-TDR-19-ADD-1, 2012,
URL: https://cds.cern.ch/record/1451888 (cit. on p. 4).

[21] ATLAS Collaboration, *Performance of the ATLAS trigger system in 2015*,
Eur. Phys. J. C **77** (2017) 317, arXiv: 1611.09661 [hep-ex] (cit. on p. 4).

[22] ATLAS Collaboration, *Correlated long-range mixed-harmonic fluctuations measured in pp, pPb and low-multiplicity PbPb collisions with the ATLAS detector*, Physics Letters B **789** (2019) 444,
arXiv: 1807.02012 (cit. on p. 5).

[23] S. Agostinelli et al., *GEANT4 – a simulation toolkit*, Nucl. Instrum. Meth. A **506** (2003) 250
(cit. on pp. 5, 13).

[24] ATLAS Collaboration, *The ATLAS Simulation Infrastructure*, Eur. Phys. J. C **70** (2010) 823,
arXiv: 1005.4568 [physics.ins-det] (cit. on pp. 5, 13).

[25] S. R. Klein, J. Nystrand, J. Seger, Y. Gorbunov and J. Butterworth,
STARlight: A Monte Carlo simulation program for ultra-peripheral collisions of relativistic ions,
Comput. Phys. Commun. **212** (2017) 258, arXiv: 1607.03838 [hep-ph] (cit. on p. 5).

[26] M. Gyulassy and X.-N. Wang, *HIJING 1.0: A Monte Carlo program for parton and particle production in high-energy hadronic and nuclear collisions*, Comput. Phys. Commun. **83** (1994) 307,
arXiv: nucl-th/9502021 (cit. on p. 5).

[27] X.-N. Wang and M. Gyulassy,
HIJING: A Monte Carlo model for multiple jet production in pp, pA and AA collisions,
Phys. Rev. D **44** (1991) 3501 (cit. on p. 5).

[28] ATLAS Collaboration, *Measurement of the Sensitivity of Two-Particle Correlations in pp Collisions to the Presence of Hard Scatterings*, (2023), arXiv: 2303.17357 [nucl-ex]
(cit. on p. 5).

[29] ATLAS Collaboration, *Measurement of long-range two-particle azimuthal correlations in Z-boson tagged pp collisions at 8 and 13 TeV*, The European Physical Journal C **80** (2020) (cit. on p. 5).

[30] ATLAS Collaboration, *Measurements of long-range azimuthal anisotropies and associated Fourier coefficients for pp collisions at $\sqrt{s}$ = 5.02 and 13 TeV and p+Pb collisions at $\sqrt{s_{\mathrm{NN}}}$ = 5.02 TeV with the ATLAS detector*, Phys. Rev. C **96** (2017) 024908, arXiv: 1609.06213 [nucl-ex]
(cit. on p. 5).

[31] ATLAS Collaboration, *Measurement of forward-backward multiplicity correlations in lead-lead, proton-lead, and proton-proton collisions with the ATLAS detector*,
Phys. Rev. C **95** (6 2017) 064914 (cit. on p. 5).

[32] ATLAS Collaboration,
Exclusive dimuon production in ultraperipheral Pb+Pb collisions at $\sqrt{s_{\mathrm{NN}}} = 5.02$ *TeV with ATLAS*,
Phys. Rev. C **104** (2021) 024906, arXiv: 2011.12211 [nucl-ex] (cit. on p. 5).

[33] ATLAS Collaboration, *Photo-nuclear jet production in ultra-peripheral Pb+Pb collisions at* $\sqrt{s_{NN}} = 5.02$ *TeV with the ATLAS detector, ATLAS-CONF-2022-021*, (2022),
URL: https://cds.cern.ch/record/2806461 (cit. on p. 5).

[34] A. Salzburger, *Optimisation of the ATLAS Track Reconstruction Software for Run-2*,
ATL-SOFT-PROC-2015-056, 2015, URL: https://cds.cern.ch/record/2018442
(cit. on p. 7).

[35] ATLAS Collaboration, *Charged-particle distributions at low transverse momentum in* $\sqrt{s} = 13$ *TeV* pp *interactions measured with the ATLAS detector at the LHC*, Eur. Phys. J. C **76** (2016) 502,
arXiv: 1606.01133 [hep-ex] (cit. on p. 7).

[36] ATLAS Collaboration,
Modelling of Track Reconstruction Inside Jets with the 2016 ATLAS $\sqrt{s} = 13$ *TeV* pp *Dataset*,
ATL-PHYS-PUB-2017-016, 2017, URL: https://cds.cern.ch/record/2275639 (cit. on p. 7).

[37] *Charged-particle distributions in* $\sqrt{s} = 13$ *TeV pp interactions measured with the ATLAS detector at the LHC*, Phys. Lett. B **758** (2016) 67, arXiv: 1602.01633 [hep-ex] (cit. on p. 8).

[38] ATLAS Collaboration,
Transverse momentum, rapidity, and centrality dependence of inclusive charged-particle production in $\sqrt{s_{NN}} = 5.02$ *TeV* p + *Pb collisions measured by the ATLAS experiment*,
Phys. Lett. B **763** (2016) 313, arXiv: 1605.06436 [hep-ex] (cit. on p. 9).